

Electron beam induced current microscopy of silicon p - n junctions in a scanning transmission electron microscope

Cite as: J. Appl. Phys. **129**, 135701 (2021); doi: [10.1063/5.0040243](https://doi.org/10.1063/5.0040243)

Submitted: 11 December 2020 · Accepted: 17 March 2021 ·

Published Online: 1 April 2021 · Corrected: 8 April 2021



Aidan P. Conlan,¹  Grigore Moldovan,² Lucas Bruas,¹ Eva Monroy,³  and David Cooper^{1,a)} 

AFFILIATIONS

¹Univ. Grenoble Alpes, CEA, LETI F-38000, Grenoble, France

²Point Electronic GmbH, Halle (Saale) D-06120, Germany

³Univ. Grenoble Alpes, CEA, Grenoble INP*, IRIG, PHELIQS F-38000, Grenoble, France

^{a)}Author to whom correspondence should be addressed: david.cooper@cea.fr

ABSTRACT

A silicon p - n junction has been mapped using electron beam induced current in both a scanning transmission electron microscope (STEM) and a conventional scanning electron microscope (SEM). In STEM, the transmission of a higher energy electron beam through the thin specimen leads to better spatial resolution and a more uniform interaction volume than can be achieved in SEM. Better spatial resolution is also achieved in the thin TEM specimens as the diffusion lengths of the minority carriers are much lower than measured in bulk material due to the proximity of specimen surfaces. We further demonstrate that a positive fixed surface charge favors surface recombination of electrons in n -type silicon and induces a surface depletion region in p -type silicon. These results have been compared to off-axis electron holography measurements of the electrostatic potentials and simulations of the internal fields.

Published under license by AIP Publishing. <https://doi.org/10.1063/5.0040243>

INTRODUCTION

Electron beam induced current (EBIC) is an electron microscopy based technique that can be used to map the generation and collection of charge carriers in semiconducting materials that contain an internal electric field. It is used widely in failure analysis for mapping p - n junctions.^{1–3} The electron–hole pairs generated by a high-energy electron beam are generally annihilated via radiative recombination or a variety of non-radiative processes. However, in the presence of an electric field, the electron–hole pairs are separated, diffuse to the electrodes, and are detected as a collected current by an amplifier. By scanning the electron beam across a region of interest, the changes in collected current are measured to produce an EBIC map.

Typically, EBIC maps are acquired in a scanning electron microscope (SEM), where the acceleration voltage and electron beam current can be easily optimized for the material, feature size, and feature depth. Given the right conditions, bulk values for the minority carrier diffusion length can be extracted.^{4–6} Another reason for the widespread use of the SEM for EBIC is that, due to

the large working distance of the SEM, there is sufficient space to electrically connect the specimen. The main drawback of SEM EBIC is that the electron beam is completely absorbed by the material, resulting in a large interaction volume with a depth-dependent generation rate.^{5,7} The shape and distribution of this generation volume is the focus of many studies^{8–12} and is crucial in understanding the collected EBIC signal. This becomes a problem for the study of polycrystalline materials or nano-objects with a large surface to volume ratio, where the generation volume is far larger than the size of the feature of interest. To improve the resolution, the lateral spread of the beam can be reduced by lowering the acceleration voltage; however, this also reduces the penetration depth of the electron beam such that only surface regions are analyzed.¹³ Compared to SEM, scanning transmission electron microscopy (STEM) uses a much higher acceleration voltage (80–300 kV) which allows the incident electrons to pass through an electron transparent specimen, providing imaging with angstrom-scale spatial resolution for bright-field and high angle annular dark-field (HAADF) detectors. STEM EBIC is particularly attractive as the electrical activity of defect structures can be mapped directly and compared to high resolution

images. EBIC performed in the TEM has to date been used to map grains,^{14–16} changes in minority carrier lifetimes,¹⁷ polarization in ferroelectric thin films,^{3,18} and defects.^{19–21}

In addition to issues related to the electron beam interaction volume, the EBIC resolution is often limited by the diffusion length of carriers. In crystalline semiconductors, carriers can travel micrometers in the material before recombining^{22,23} while a depletion region can be at the scale of tens of nanometers for doped semiconductors.²⁴ Therefore, to measure the depletion region with improved spatial resolution, it is necessary to minimise the diffusion length of carriers outside the junction while ensuring that the internal electric field is not destroyed during specimen preparation. To meet this challenge, we have observed specimens with total thicknesses in the range from 350 nm to 1 μm using focused ion beam (FIB) milling and demonstrate the effect of the specimen surfaces on the resolution of the technique. These EBIC results are confirmed by both off-axis electron beam holography (from now referred to as electron holography) and simulations.

EXPERIMENT

The sample examined was a symmetrically doped $1 \times 10^{19} \text{ cm}^{-3}$ silicon p - n junction, comprising a 1 μm n -type phosphorus doped layer on a 1 μm p -type boron doped layer, grown on a lightly p -doped Si(100) substrate by metal-organic chemical vapour deposition. This structure has been extensively characterized elsewhere by electron holography and differential phase contrast STEM.^{25–27}

A straightforward and reproducible methodology has been developed to be compatible with a Protochips Aduro 500 TEM holder. Here, a silicon half-chip with patterned electrical contacts is used such that the same specimen can be examined in a TEM or SEM. A specimen containing the p - n junction was prepared by *in situ* lift-out using a FEI Strata 400 Dual Beam FIB system. To improve the measured EBIC signal, metal contacts were deposited at the top and bottom surfaces of the lamella. Ion beam deposited contacts are highly conductive due to the presence of Ga implanted at normal incidence into the amorphized silicon surface during the ion beam assisted deposition (IBAD) of the metallic tungsten.

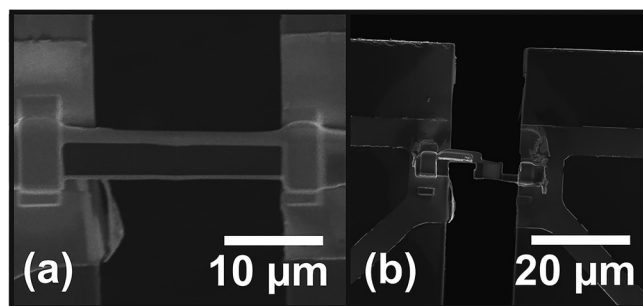


FIG. 1. FIB lamella preparation for in situ biasing. (a) A specimen is prepared by *in situ* lift out and metal deposited to the top and bottom by rotating the specimen in the FIB on a dedicated holder. (b) The lamella is then milled to different thicknesses, and as a last step, isolation cuts are made such that the current passes through the region of interest.

Figure 1(a) shows a lamella with both top and bottom parallel tungsten electrodes. To achieve this, a conventional lift out using 30 kV Ga^+ ions is performed and then welded by IBAD onto a rotatable probe. The probe is rotated 90° so that the amorphous base of the lamella is removed at normal incidence and then rotated by a further 90° such that an additional tungsten electrode can be deposited. The lamella is then transferred and welded to the electrical biasing chip. The specimen is polished to different final thicknesses with 16 kV ions. Figure 1(b) shows how cuts at the edges of the lamella are made to isolate the p - n junction and complete the desired electrical circuit. As a final step, the specimen is cleaned using 2 kV ions to reduce the effect of the conducting Ga-implanted surfaces. For these experiments, the “half-chip” was developed such that the specimen can quickly and easily be placed onto the electrical contacts from above using an Omniprobe operated in a standard FIB configuration.

As most EBIC is SEM-based and is typically performed top-down on as-grown wafers,²⁸ or on the sides of cleaved wafers,²⁹ it is necessary to understand the effects of observing very thin TEM specimens. Electron holography was performed to assess the effects of specimen preparation on the specimen surfaces and provide additional information about the electrostatic potentials. Differential phase contrast (DPC) based techniques could also be used to observe the electric fields in doped specimens, either using a segmented²⁶ or pixelated detector.²⁷ Electron holography was chosen here as the slowly changing electrical potentials at the specimen surfaces will lead to very weak electric fields, which would be difficult to detect by DPC based methods. Figure 2(a) shows a schematic for electron holography. An electron biprism is used to interfere an object wave with a reference wave to form an interference pattern, known as the hologram. By performing a simple Fourier reconstruction technique, a phase map can be obtained that in the absence of magnetic fields and dynamical diffraction, directly provides information about the electrostatic potential in a specimen.³⁰ Equation (1) shows that, in the absence of magnetic field, the phase, $\phi(\mathbf{r})$, of an electron travelling along the z direction is sensitive to the electrostatic potential, $V(\mathbf{r})$,

$$\phi(\mathbf{r}) = \frac{e}{\hbar v} \int_{-\infty}^{+\infty} V(\mathbf{r}) dz, \quad (1)$$

where e is the electron charge, v is the electron velocity, and \hbar is the reduced Planck's constant.³¹ Electron holograms were acquired using a FEI Titan Ultimate operated at 200 kV. To obtain a large field of view of 1.4 μm , a Lorentz lens was used. Electron holograms with a fringe spacing of 3 nm were reconstructed to provide a spatial resolution of 6 nm. Then to improve the sensitivity, a stack of 16 holograms was acquired and summed using the Holoview software.³² For each specimen, the crystalline thickness was measured by two-beam convergent beam electron diffraction analysis.^{25,27} For these experiments, it was necessary to prepare different specimens than for the EBIC experiments as a vacuum reference region is required.

To compare the STEM EBIC to standard SEM EBIC mapping, experiments were performed in a Zeiss Merlin SEM using 5, 10,

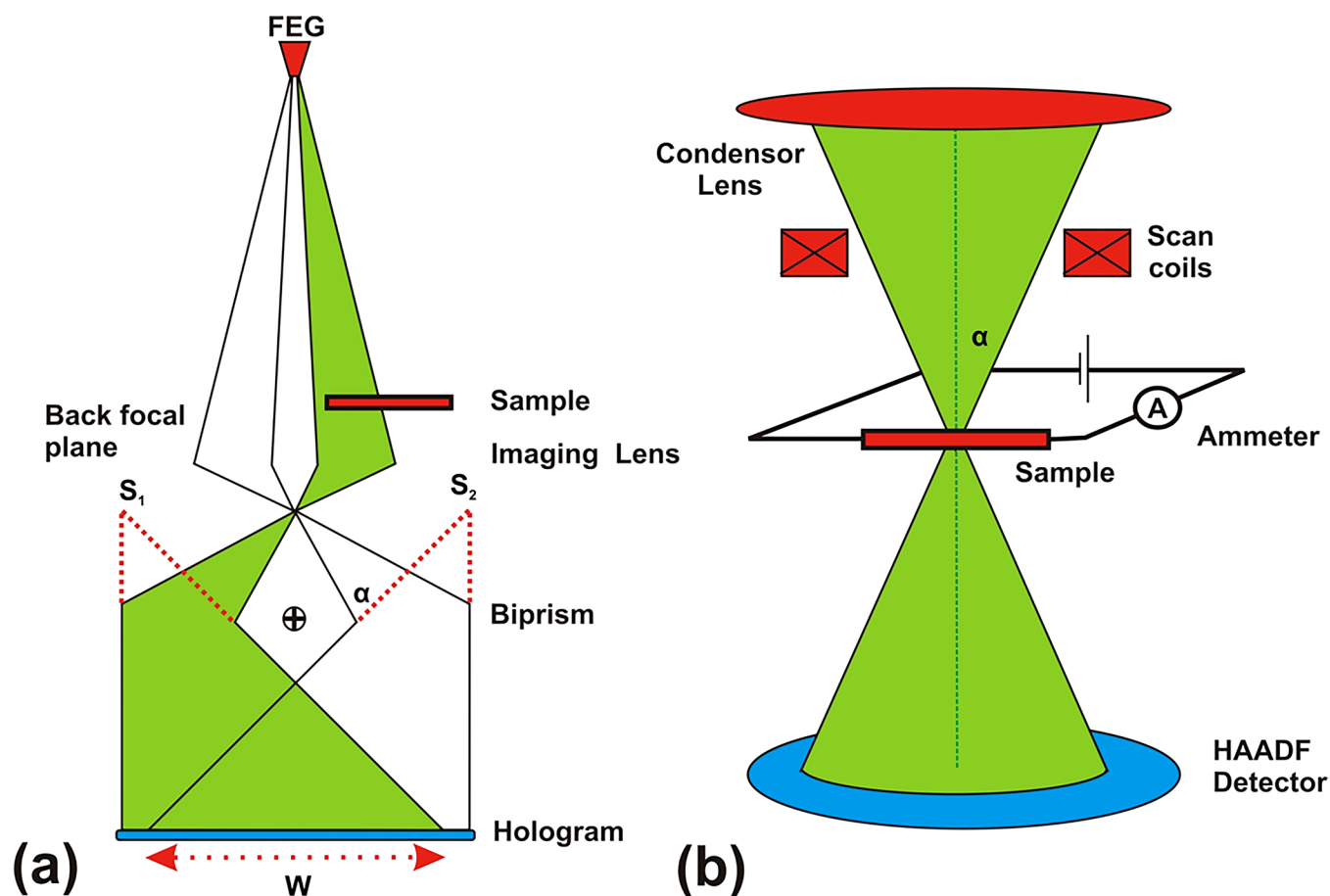


FIG. 2. (a) Schematic of the optical setup for off-axis electron holography and (b) EBIC.

and 30 kV acceleration voltages with 100 pA beam current, using a dedicated Protochips specimen holder. Images formed from secondary electron emission were acquired simultaneously with the EBIC maps. The same sample was then studied in a FEI Titan Ultimate aberration-corrected (S)TEM microscope operated at 200 kV with a beam current of 1 nA and a convergence angle of 31 mrad using a point electronic GmbH EBIC system. The number of excited electron-hole pairs generated per beam electron drops by approximately an order of magnitude when going from 10 kV electrons to 200 kV electrons, meaning higher beam currents are required to get a signal in STEM EBIC. For these experiments, the generation rate was found to be approximately 600 and 30 electron-hole pairs for SEM and STEM EBIC, respectively. To further improve the collected current signal over electrical noise, a dwell time of 69 μ s per pixel was used for 1024×1024 pixels (80 s per image). STEM HAADF images were acquired simultaneously by capturing scattered electrons with an annular detector placed below the specimen. Figure 1(b) shows a schematic of the experimental setup where the beam is scanned across the specimen and an electric current is locally measured at each point.

Simulations of high energy electron collisions in silicon of different thicknesses were calculated using the PENELOPE³³ and CASINO³⁴ Monte Carlo codes. The trajectories of 1000 electrons in a 1 nm diameter probe were simulated with an absorption threshold of 50 eV in a 350 nm-thick silicon layer in vacuum for 5, 10, 30, and 200 kV electrons to estimate the generation volume of electron-hole pairs. The simulation with the same parameters was repeated for 200 kV electrons incident on a 1000 nm-thick silicon layer to find the effect of specimen thickness. Two-dimensional (2D) simulations of the electric field in the specimen were then performed using the Nextnano software.³⁵ A p - n junction was modelled with the nominal doping levels within a 350 nm thick lamella with surfaces perpendicular to the junction. Due to the FIB preparation, this time with the incident Ga ions at glancing incidence, we consider that the surfaces are amorphized (modelled as intrinsic silicon) to a depth of 15 nm. This model does not include the damaged crystalline sub-surfaces arising from cascade collisions during FIB milling. From observations made by electron holography, a positive surface charge of $5 \times 10^{13} \text{ cm}^{-2}$ was used to account for secondary electron emission. This fixed positive charge follows

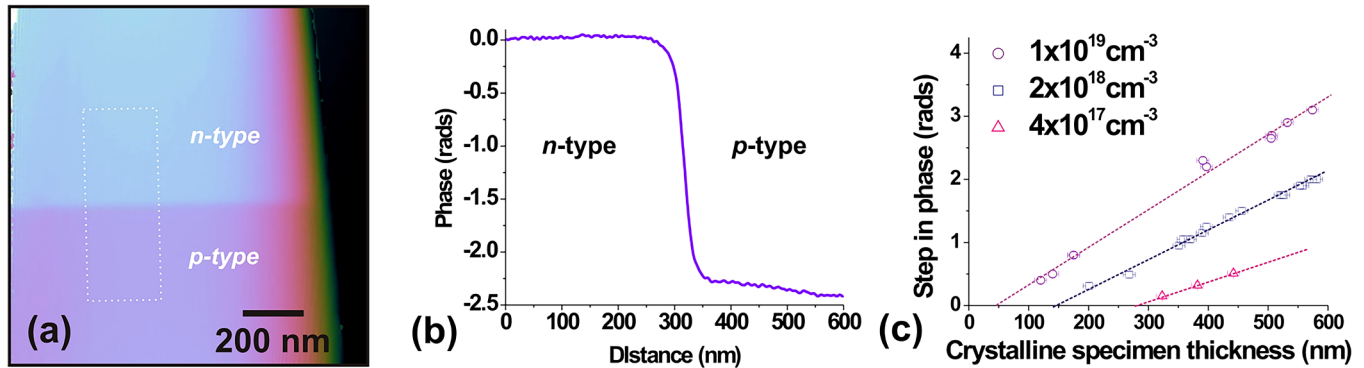


FIG. 3. (a) Phase image of a specimen containing a p–n junction. (b) The measured phase across the junction. (c) The step in phase measured across silicon p–n junctions in TEM specimens with different crystalline thicknesses and different dopant concentrations. The surface depletion layer thickness can be inferred from the x-intercept.

a Gaussian distribution with its maximum at the crystalline/amorphous interface and extends 15 nm inside the lamella. Then, the electric field in the specimen was calculated by solving Poisson's equation.

RESULTS AND DISCUSSION

Figure 3(a) shows a phase image of a 391 nm thick specimen containing a p–n junction obtained by electron holography. Strong phase contrast can be seen between the p-type and n-type regions. The electrical junction does not extend all the way to the specimen edge due to the surface depletion layer which arises from FIB damage at the specimen surfaces, specimen charging from electron beam irradiation and secondary electron (SE) emission.^{25,36,37} The surface depletion layer is expected to be present on the top and bottom surfaces of the thin TEM specimen. The surface effects are more prominent in the n-type side of the specimen compared to the p-type side due to the SE emission, which leaves a positively charged surface layer. Figure 3(b) shows a phase profile measured across the junction shown in Fig. 3(a) averaged across the indicated region. A step in phase of 2.3 ± 0.05 rad is measured. To quantify the effect of the charged surfaces on the total measured potential across the junction, the step in phase can be plotted as a function of the crystalline thickness. From the x-intercept the surface depletion layer can be inferred, being the crystalline thickness of specimen where no signal from the p–n junction is measured. Figure 3(c) shows the results acquired in this experiment, adding one data point to some previously acquired

data for the step in phase measured across many different TEM specimens containing p–n junctions with different dopant concentrations,²⁵ and Table I shows the surface depletion thickness as a function of the dopant concentration. Here, higher dopant concentrations have lower values of the surface depletion thickness,³⁸ due to the smaller depletion region induced by the surface charges. Conversely, when looking at specimens with low dopant concentrations, very thick specimens would be required in order to measure the junction as the surface depletion layer is much higher.

Following the electron holography experiments, a specimen with four regions of different thickness (350, 390, 535, and 1000 nm) was prepared. This large range of thicknesses were chosen to ensure that an EBIC signal would be measured despite the surface effects. SEM-based EBIC experiments were performed on the specimen at different operating voltages of 5, 10, and 30 kV. Figures 4(a) and 4(b) show secondary electron and EBIC maps for 5 kV electrons, respectively. Interestingly, contrast between the doped regions can be clearly seen in the secondary electron images made at low operating voltages, which has been observed elsewhere.^{39,40} For the EBIC map, bright contrast is observed in the region of the electrical junction, which appears wider in the thicker parts of the specimen. Intensity profiles extracted from across the 350 nm thick specimen are plotted in Fig. 4(c) for different operating voltages. It is well known that the spatial resolution in EBIC is limited by the effective diffusion length of minority charge carriers outside of the depletion region. This causes an exponential decay in the EBIC signal from the edge of the depletion region, which is best seen using a normalized semilog plot. The linear trends in the EBIC signal reveal regions governed by carrier diffusion as opposed to carrier drift which is dominant in the depletion region. Inspection of the intensity profiles shows that the spatial resolution of SEM EBIC changes with operating voltage. This can be quantified by fitting the equation for EBIC current, I_{EBIC} , and extracting the effective diffusion length of minority carriers, L_{eff}

$$I_{EBIC} = kx^\alpha e^{-\frac{x}{L_{eff}}}, \quad (2)$$

TABLE I. The measured surface depletion layer thickness as a function of the dopant concentration for symmetrically doped silicon p–n junctions.

Dopant concentration (cm^{-3})	Surface depletion layer thickness (nm)
1×10^{19}	60 ± 15
2×10^{18}	140 ± 15
4×10^{17}	250 ± 15

where x is the distance from the space-charge region, and k and α are both fitting constants.^{13,41}

The effective diffusion lengths of minority electrons in the p -region are shown in Fig. 4(d). They have been extracted by fitting Eq. (1) using the method of least-squares to the linear p -region of the EBIC profiles in Fig. 4(c). The sensitivity of the result to the operating voltage reveals its impact on the resolution of the measurement. To understand better this trend, it is important to consider the effect of the specimen surfaces and the interaction volume of the electron beam. Trajectories of the electron beam in the specimen were calculated using the CASINO Monte Carlo code. Figure 5 shows the distribution of collisions for 5, 10, 30, and 200 kV electrons in 350 nm silicon. In a thin specimen, the carrier diffusion length is significantly reduced due to surface recombination.²⁹ For a low operation voltage of 5 kV, the electrons create a

generation volume of electron-hole pairs concentrated close to the point of incidence. Figure 5(a) shows that the surface recombination is slightly overestimated due to the in-plane size of the electron interaction volume. For intermediate voltages such as 10 kV, the electron interaction volume increases both in the normal direction and in-plane as shown in Fig. 5(b), which degrades the resolution of the measurement and can lead to a significant overestimation of the diffusion length. Figure 5(c) shows that, at even higher voltages of 30 kV, most of the beam transmits through the specimen. Here the electron trajectories in the specimen shorten in both depth and breadth with decreasing operation voltage. Extending this analysis to very high voltages such as 200 kV in Fig. 5(d), we measure the minority carrier diffusion length in the sample with minimum error as nearly all the primary electrons transmit through the thickness of the specimen.

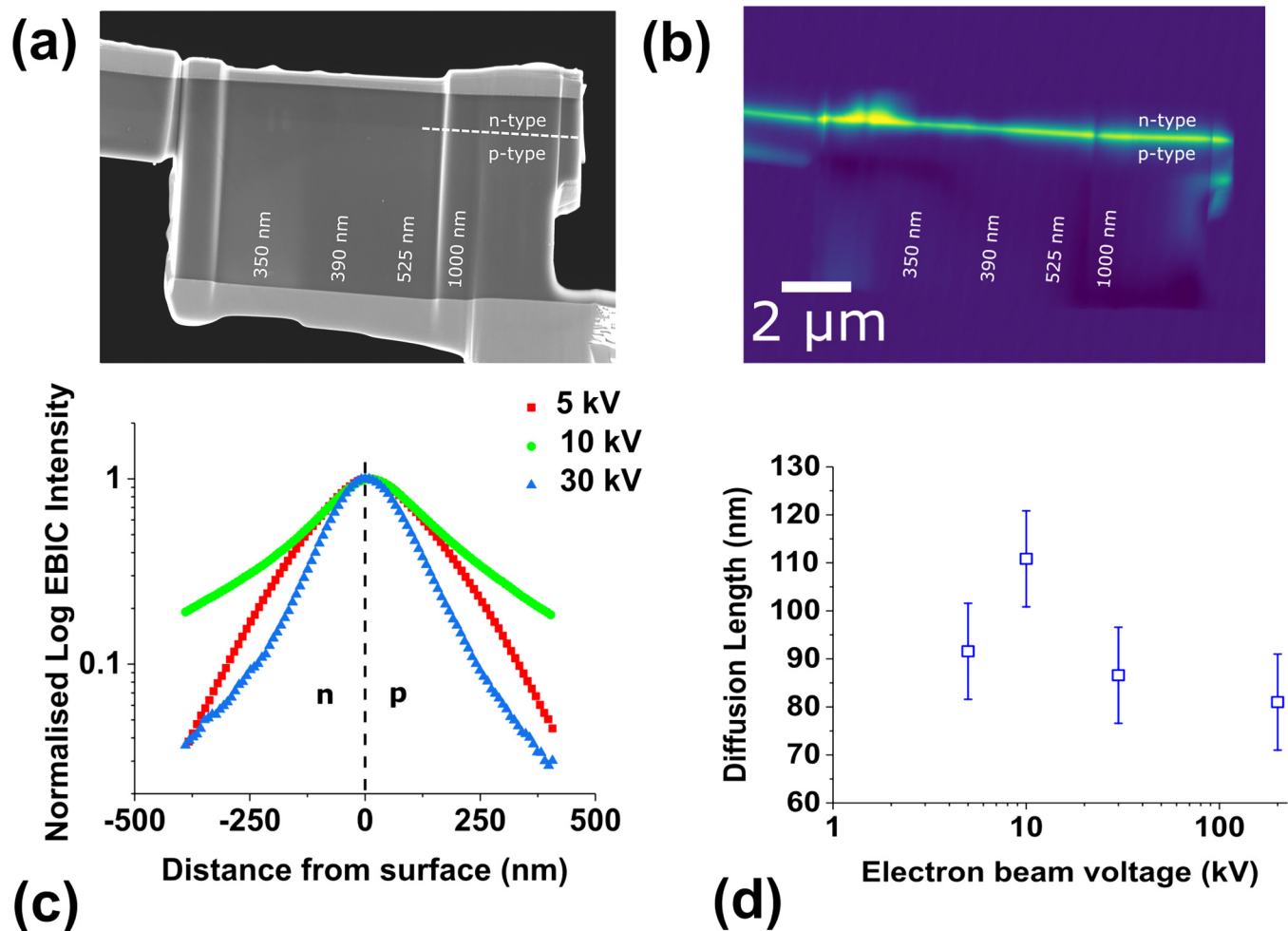


FIG. 4. (a) SEM SE image and (b) EBIC image of the specimen acquired at 5 kV. All scale bars are $1\ \mu\text{m}$. (c) EBIC intensity profiles across the p - n junction region for different SEM beam energies, plotted semilog to show the change in diffusion length near the depletion zone. (d) Effective minority carrier diffusion length extracted from the linear p -type region in (c) for different beam energies.

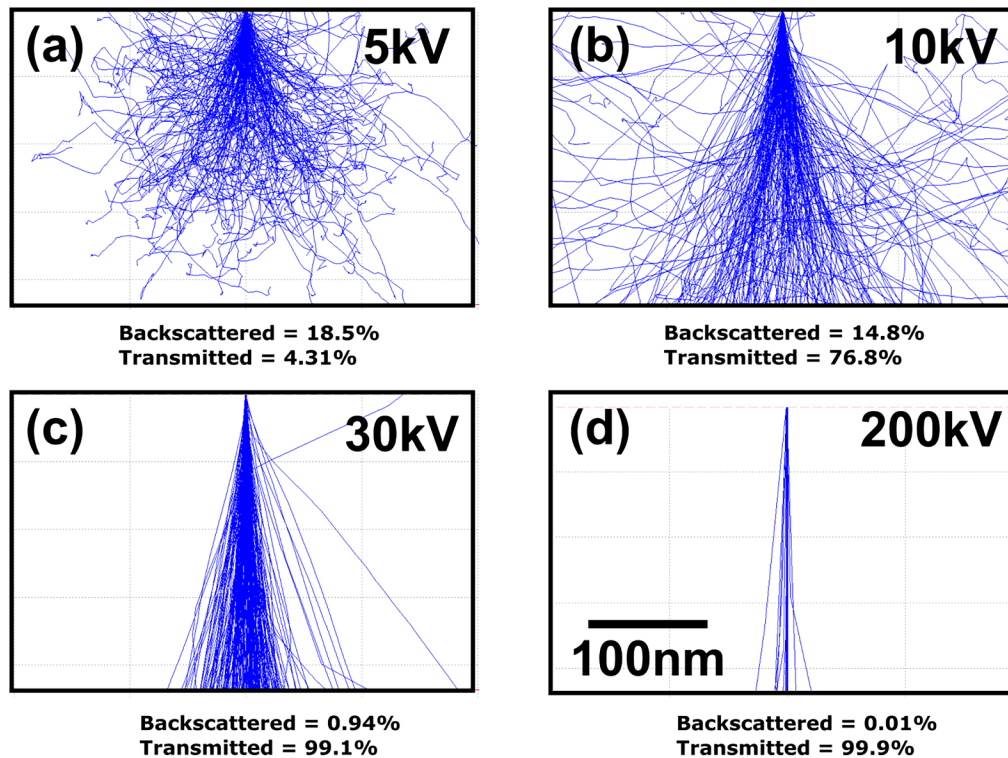


FIG. 5. Trajectories of (a) 5, (b) 10, (c) 30, and (d) 200 kV primary beam electrons in 350 nm thick Silicon, as predicted by the CASINO Monte Carlo simulation package. All scale bars 100 nm.

Figures 6(a) and 6(b) show HAADF STEM images of the specimen acquired at 200 kV. The junction is not visible in the STEM HAADF images as a dopant concentration of $1 \times 10^{19} \text{ cm}^{-3}$ boron and phosphorous atoms corresponds to a percentage of only

0.02% in silicon which is not detectable here. Figure 6(c) shows the STEM EBIC map, which reveals the position of the p - n junction in all regions. The intensity and width of the EBIC signal at the p - n junction varying for different thicknesses can also be seen. The

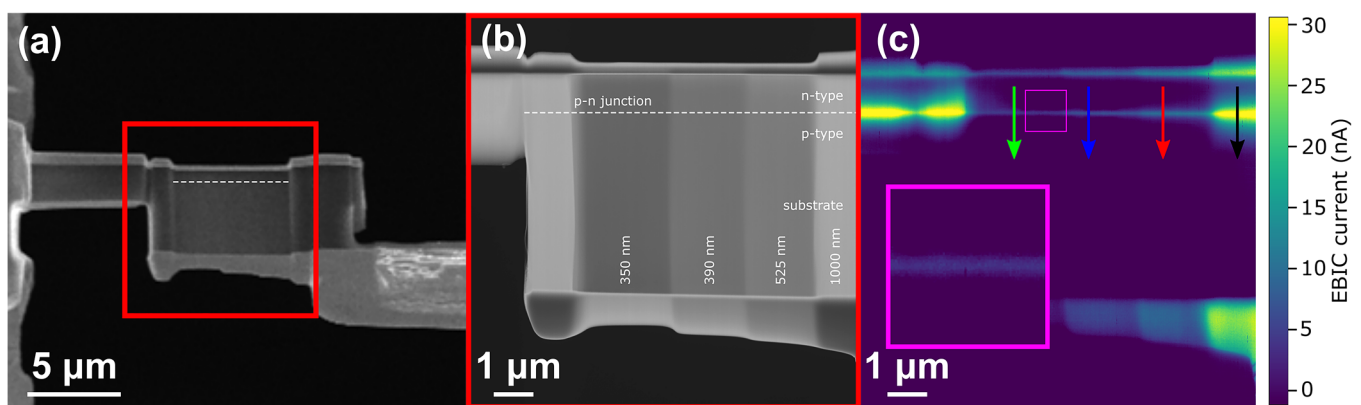


FIG. 6. (a) SEM image of the cross section specimen milled and polished to different thicknesses by FIB. The junction is marked by the dashed line. (b) STEM HAADF image showing the two tungsten electrodes above and below the silicon lamella. The n and p doped regions are shown either side of the junction (marked by a dashed line). (c) STEM EBIC with the same field of view. The junction can be clearly resolved $1 \mu\text{m}$ below the silicon surface. (d) The inset shows the junction at higher magnification in the thinnest region of the specimen with a field of view of $1 \mu\text{m}$.

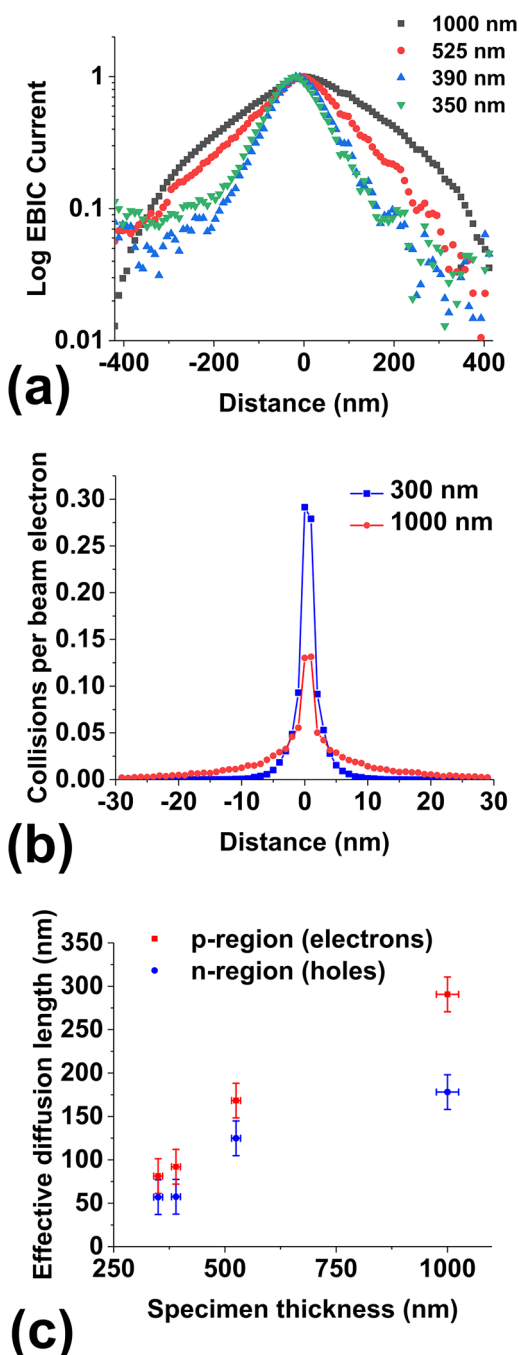


FIG. 7. The effect of specimen thickness on STEM EBIC resolution (a) Semi-logarithmic plot of normalised EBIC intensity profiles extracted across the p - n junction for regions of different thickness. (b) The lateral spread of collisions from 200 kV electrons in 300 nm and 1000 nm-thick silicon, calculated by the PENELOPE Monte Carlo code. (c) Effective minority carrier diffusion lengths for the p - and n -doped regions (minority electrons and holes, respectively) estimated for each specimen thickness.

tungsten electrodes are visible due to secondary electron emission beam absorbed current (SEEBIC), which results from the collection of secondary holes left behind by electron emission. This is also present but not visible in the SEM EBIC maps as the generation of carriers in the junction is very high compared to the SEEBIC signal. Thus, when performing EBIC in a TEM using higher energy electrons, it is necessary to increase the amplification of the signal and the SEEBIC current has a magnitude comparable to that generated in the electrical junction. SEEBIC has strong mass-thickness contrast and is brightest where tungsten is thickest in the direction of the electron beam.

Figure 7(a) shows the EBIC intensity profiles across the junction extracted along the regions indicated by the arrows in Fig. 6(c). The data are normalized to each maximum value and is presented on a semi-logarithmic scale. The intensity profiles have been compared to the spatial resolution of the system, which for electron microscopy techniques is generally limited by the probe size and interaction volume. Figure 7(b) shows Monte Carlo simulations for the beam spreading in the thinnest and thickest specimen volumes examined here, indicating that even in the thickest region the lateral spread of the electron collisions is only significant to a radius of 30 nm from the point of beam incidence. In the case of a 350 nm-thick specimen, the lateral spread would be reduced to a radius of 10 nm. These values are much smaller than the decays observed in the SEM EBIC profiles in Fig. 4(c). Here, we again fit Eq. (1) to the linear regions of Fig. 7(a) to extract the effective minority carrier diffusion length for both n and p regions, plotted in Fig. 7(c).

The effective diffusion length increases with specimen thickness as surface recombination becomes less dominant. For example, in the p -type material, the n -type minority carrier diffusion lengths have been measured as 290 ± 20 nm and 81 ± 20 nm for the 1000 nm and 350 nm thick specimens, respectively. For the n -type material, values of 178 ± 20 nm and 57 ± 20 nm were obtained for the same thicknesses. From literature, a silicon p - n junction specimen symmetrically doped to $1 \times 10^{19} \text{ cm}^{-3}$ should have a bulk diffusion length of minority electrons and holes of approximately 4500 and 2250 nm, respectively.^{22,23} These values for bulk diffusion length are an order of magnitude larger than those that we measure in our specimen. This behaviour is typical of structures where transport is constrained by surface phenomena, as is well known in the case of silicon nanowires,⁴² where surface recombination can shorten the carrier lifetime by 4–5 orders of magnitude. On the other hand, these measurements have also revealed that the effective minority carrier diffusion lengths in the n -type material are systematically lower than in the p -type material.

Electron holography results have already demonstrated the presence of an electrical modification arising from FIB specimen preparation and subsequent exposure to the electron beam. However, surface effects are also observed by STEM EBIC. Figure 8(a) shows a STEM EBIC image of an edge region of a different FIB lamella (1 μm thick) prepared from the same wafer. At the specimen edge in the n -type region, a localized bright line is observed where SEEBIC signal is collected from redeposited material. However, at the p -surface, a current that decreases exponentially from the surface to the bulk material is seen which is not present in the n -type region. These EBIC results are reproduced by

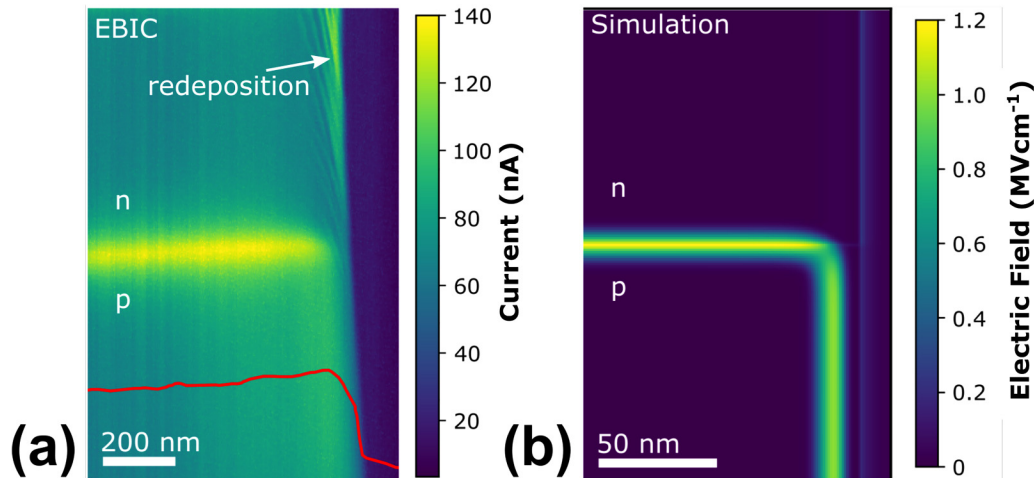


FIG. 8. (a) Experimental EBIC map showing the specimen edge. (b) Simulation of the electric field in the specimen.

the simulated field map shown in Fig. 8(b). Following the electron holography results, a fixed positive charge is applied to the surface and this charge repels the mobile holes in the *p*-type region of the specimen to create a space charge region at the surface. On the contrary, in the *n*-type region, the positive surface charge attracts electrons toward the surface, favoring surface recombination.⁴³ This explains why, despite the bulk diffusion length for electrons being twice that of holes, we observe the values of effective diffusion lengths of electrons and holes begin to converge in the thinnest (350 nm) silicon region, where values of 81 nm for the minority carriers in the *p*-type material were obtained compared to 57 nm in the *n*-type material.

CONCLUSION

We have used SEM and STEM EBIC to map the position of a *p*-*n* junction in FIB-prepared silicon lamellas with thicknesses in the range of 350–1000 nm. During these experiments, the effects of charged surfaces compete with the collection of excited carriers. By changing the electron beam energy we find that the *p*-*n* junction can be mapped with different spatial resolutions, with 200 kV giving the best results. This is explained by the fact that high energy electrons are able to traverse the whole thickness of the specimen with minimum in-plane spread, thus accurate quantification of the minority carrier diffusion length is possible for STEM EBIC. It was found that, by using a specimen with thickness of less than 1 μm , surface recombination reduces the effective diffusion lengths for minority electrons and holes from their bulk values (4500 nm and 2250 nm, respectively) to less than 300 nm, with 57–81 nm being measured in the thinnest region. We also find from the ratio between electron and hole diffusion lengths, higher losses are observed in the case of electrons. These variations are attributed to the presence of fixed positive charges at the surface, which generate surface band-bending and forcing electrons to be

preferentially recombined. The presence of charged surfaces was also confirmed by electron holography.

The use of STEM EBIC opens new opportunities in semiconductor characterisation by linking the distribution of electric fields and defect structures using the high spatial resolutions available in a TEM to the electrical properties of a device measured *in situ*. Additional advantages of using this TEM-based approach is the availability to high-resolution structural imaging, composition, and field mapping using complementary techniques on the same samples. This method of applying EBIC to semiconductors will have many additional applications in the study of other low-dimensional systems such as nanowires and 2D materials, as well as in all doped semiconductor devices for optoelectronics and photovoltaic applications. Further work is required to improve the sensitivity of the technique and provide optimized specimen geometries for different materials systems.

ACKNOWLEDGMENTS

This work, done on the NanoCharacterisation PlatForm (PFNC), was supported by the “Recherches Technologiques de Base” Program of the French Ministry of Research. We acknowledge financial support of the Cross-Disciplinary Program on Instrumentation and Detection of CEA, the French Alternative Energies and Atomic Energy Commission.

DATA AVAILABILITY

The data that support the findings of this study are available from the corresponding author upon reasonable request.

REFERENCES

- ¹J.-M. Bonard and J.-D. Ganière, *J. Appl. Phys.* **79**, 6987 (1996).
- ²S. I. Maximenko, M. P. Lumb, R. Hoheisel, M. Gonzalez, D. A. Scheiman, S. R. Messenger, T. N. D. Tibbits, M. Imaizumi, T. Ohshima, S. I. Sato, P. P. Jenkins, and R. J. Walters, *J. Appl. Phys.* **118**, 245705 (2015).

- ³M.-G. Han, J. A. Garlow, M. S. J. Marshall, A. L. Tiano, S. S. Wong, S.-W. Cheong, F. J. Walker, C. H. Ahn, and Y. Zhu, *Ultramicroscopy* **176**, 80 (2017).
- ⁴E. B. Yakimov, *J. Alloys Compd.* **627**, 344 (2015).
- ⁵O. Marcelot and P. Magnan, *Ultramicroscopy* **197**, 23 (2019).
- ⁶Z. Taghipour, S. Lee, S. A. Myers, E. H. Steenbergen, C. P. Morath, V. M. Cowan, S. Mathews, G. Balakrishnan, and S. Krishna, *Phys. Rev. Appl.* **11**, 024047 (2019).
- ⁷N. Yoon, C. J. Reynier, G. Ariyawansa, J. M. Duran, J. E. Scheihing, J. Mabon, and D. Wasserman, *J. Appl. Phys.* **122**, 074503 (2017).
- ⁸K. L. Luke, *J. Appl. Phys.* **90**, 3413 (2001).
- ⁹C. M. Parish and P. E. Russell, *Appl. Phys. Lett.* **89**, 192108 (2006).
- ¹⁰O. Kurniawan and V. K. S. Ong, *IEEE Trans. Electron Devices* **56**, 1094 (2009).
- ¹¹O. Kurniawan, C. C. Tan, V. K. S. Ong, E. Li, and C. J. Humphreys, *IEEE Trans. Electron Devices* **57**, 2455 (2010).
- ¹²J. E. Moore, C. A. Affouda, S. I. Maximenko, and P. Jenkins, *J. Appl. Phys.* **124**, 113102 (2018).
- ¹³G. Moldovan, P. Kazemian, P. R. Edwards, V. K. S. Ong, O. Kurniawan, and C. J. Humphreys, *Ultramicroscopy* **107**, 382 (2007).
- ¹⁴S. Tanaka, H. Tanaka, T. Kawasaki, M. Ichihashi, T. Tanji, K. Arafune, Y. Ohshita, and M. Yamaguchi, *J. Mater. Sci. Mater. Electron.* **19**, 324 (2008).
- ¹⁵W. A. Hubbard, M. Mecklenburg, H. L. Chan, and B. C. Regan, *Phys. Rev. Appl.* **10**, 044066 (2018).
- ¹⁶M. Mecklenburg, W. A. Hubbard, J. J. Lodico, and B. C. Regan, *Ultramicroscopy* **207**, 112852 (2019).
- ¹⁷T. Kushida, S. Tanaka, C. Morita, T. Tanji, and Y. Ohshita, *Microscopy* **61**, 293 (2012).
- ¹⁸M. G. Han, M. S. J. Marshall, L. Wu, M. A. Schofield, T. Aoki, R. Twisten, J. Hoffman, F. J. Walker, C. H. Ahn, and Y. Zhu, *Nat. Commun.* **5**, 3461 (2014).
- ¹⁹T. Meyer, B. Kressdorf, J. Lindner, P. Peretzki, V. Roddatis, C. Jooss, and M. Seibt, *J. Phys. Conf. Ser.* **1190**, 012009 (2019).
- ²⁰C. Li, J. Poplawsky, Y. Wu, A. R. Lupini, A. Mouti, D. N. Leonard, N. Paudel, K. Jones, W. Yin, M. Al-Jassim, Y. Yan, and S. J. Pennycook, *Ultramicroscopy* **134**, 113 (2013).
- ²¹C. L. Progl, C. M. Parish, J. P. Vitarelli, and P. E. Russell, *Appl. Phys. Lett.* **92**, 242103 (2008).
- ²²J. A. del Alamo and R. M. Swanson, *Solid State Electron.* **30**, 1127 (1987).
- ²³M. S. Tyagi and R. Van Overstraeten, *Solid State Electron.* **26**, 577 (1983).
- ²⁴D. Ban, E. H. Sargent, St. J. Dixon-Warren, I. Calder, A. J. SpringThorpe, R. Dworschak, G. Este, and J. K. White, *Appl. Phys. Lett.* **81**, 5057 (2002).
- ²⁵D. Cooper, C. Ailliot, R. Truche, J.-P. Barnes, J.-M. Hartmann, and F. Bertin, *J. Appl. Phys.* **104**, 064513 (2008).
- ²⁶B. Haas, J.-L. Rouvière, V. Boureau, R. Berthier, and D. Cooper, *Ultramicroscopy* **198**, 58 (2019).
- ²⁷L. Bruas, V. Boureau, A. P. Conlan, S. Martinie, J.-L. Rouvière, and D. Cooper, *J. Appl. Phys.* **127**, 205703 (2020).
- ²⁸O. Marcelot, S. I. Maximenko, and P. Magnan, *IEEE Trans. Electron Devices* **61**, 2437 (2014).
- ²⁹R. Zhou, M. Yu, D. Tweddle, P. Hamer, D. Chen, B. Hallam, A. Ciesla, P. P. Altermatt, P. R. Wilshaw, and R. S. Bonilla, *J. Appl. Phys.* **127**, 024502 (2020).
- ³⁰H. Lichte and M. Lehmann, *Rep. Prog. Phys.* **71**, 016102 (2008).
- ³¹A. Tonomura, *Electron Holography* (Springer, Berlin, 1999).
- ³²V. Boureau, R. McLeod, B. Mayall, and D. Cooper, *Ultramicroscopy* **193**, 52 (2018).
- ³³P. T. Pinard, H. Demers, F. Salvat, R. Gauvin, J. M. Fernández-Varea, E. Acosta, J. Sempau, and X. L. Lovet, PyPENELOPE (2012), available at <http://pypenelope.sourceforge.net>.
- ³⁴D. Drouin, A. R. Couture, D. Joly, X. Tastet, V. Aimez, and R. Gauvin, *Scanning* **29**, 92 (2007).
- ³⁵S. Birner, T. Zibold, T. Andlauer, T. Kubis, M. Sabathil, A. Trellakis, and P. Vogl, *IEEE Trans. Electron Devices* **54**, 2137 (2007).
- ³⁶S. Rubanov and P. R. Munroe, *J. Microsc.* **214**, 213 (2004).
- ³⁷J. Cazaux, *Nucl. Instrum. Methods Phys. Res. Sect. B* **244**, 307 (2006).
- ³⁸D. Cooper, P. Rivallin, J.-M. Hartmann, A. Chabli, and R. E. Dunin-Borkowski, *J. Appl. Phys.* **106**, 064506 (2009).
- ³⁹C. P. Sealy, M. R. Castell, and P. R. Wilshaw, *J. Electron Microsc.* **49**, 311 (2000).
- ⁴⁰P. Kazemian, S. A. M. Mentink, C. Rodenburg, and C. J. Humphreys, *J. Appl. Phys.* **100**, 054901 (2006).
- ⁴¹V. K. S. Ong, *Rev. Sci. Instrum.* **69**, 1814 (1998).
- ⁴²J. E. Allen, E. R. Hemesath, D. E. Perea, J. L. Lensch-Falk, Z. Y. Li, F. Yin, M. H. Gass, P. Wang, A. L. Bleloch, R. E. Palmer, and L. J. Lauhon, *Nat. Nanotechnol.* **3**, 168 (2008).
- ⁴³P. M. Haney, H. P. Yoon, B. Gaury, and N. B. Zhitenev, *J. Appl. Phys.* **120**, 095702 (2016).